Journal of Neuroscience Methods 403 (2024) 110037

Contents lists available at ScienceDirect

Journal of Neuroscience Methods

journal homepage: www.elsevier.com/locate/jneumeth

Influence of threshold selection and image sequence in in-vivo segmentation of enlarged perivascular spaces

Maria del C. Valdés Hernández [a,*], Roberto Duarte Coello [a], William Xu [b], José Bernal [a,c,d], Yajun Cheng [e], Lucia Ballerini [a,f], Stewart J. Wiseman [a], Francesca M. Chappell [a], Una Clancy [a], Daniela Jaime García [a], Carmen Arteaga Reyes [a], Jun-Fang Zhang [a,g], Xiaodi Liu [h], Will Hewins [a], Michael Stringer [a], Fergus Doubal [a], Michael J. Thrippleton [a], Angela Jochems [a], Rosalind Brown [a], Joanna M. Wardlaw [a]

[a] Centre for Clinical Brain Sciences, Department of Neuroimaging Sciences, University of Edinburgh, Edinburgh, UK
[b] College of Medicine and Veterinary Medicine, University of Edinburgh, Edinburgh, UK
[c] German Centre for Neurodegenerative Diseases (DZNE), Magdeburg, Germany
[d] Institute of Cognitive Neurology and Dementia Research, Otto-von-Guericke University Magdeburg, Magdeburg, Germany
[e] Department of Neurology, West China Hospital of Sichuan University, Chengdu, China
[f] University for Foreigner of Perugia, Perugia, Italy
[g] Department of Neurology, Shanghai General Hospital, Shanghai Jiao Tong University School of Medicine, Shanghai, China
[h] Division of Neurology, Department of Medicine, The University of Hong Kong, Hong Kong

ARTICLE INFO

Keywords:
Perivascular spaces
Virchow-Robin spaces
Small vessel disease
White matter hyperintensities
Lacunes
MRI
Brain

ABSTRACT

Background: Growing interest surrounds perivascular spaces (PVS) as a clinical biomarker of brain dysfunction given their association with cerebrovascular risk factors and disease. Neuroimaging techniques allowing quick and reliable quantification are being developed, but, in practice, they require optimisation as their limits of validity are usually unspecified.

New method: We evaluate modifications and alternatives to a state-of-the-art (SOTA) PVS segmentation method that uses a vesselness filter to enhance PVS discrimination, followed by thresholding of its response, applied to brain magnetic resonance images (MRI) from patients with sporadic small vessel disease acquired at 3 T.

Results: The method is robust against inter-observer differences in threshold selection, but separate thresholds for each region of interest (i.e., basal ganglia, centrum semiovale, and midbrain) are required. Noise needs to be assessed prior to selecting these thresholds, as effect of noise and imaging artefacts can be mitigated with a careful optimisation of these thresholds. PVS segmentation from T1-weighted images alone, misses small PVS, therefore, underestimates PVS count, may overestimate individual PVS volume especially in the basal ganglia, and is susceptible to the inclusion of calcified vessels and mineral deposits. Visual analyses indicated the incomplete and fragmented detection of long and thin PVS as the primary cause of errors, with the Frangi filter coping better than the Jerman filter.

Comparison with existing methods: Limits of validity to a SOTA PVS segmentation method applied to 3 T MRI with confounding pathology are given.

Conclusions: Evidence presented reinforces the STRIVE-2 recommendation of using T2-weighted images for PVS assessment wherever possible. The Frangi filter is recommended for PVS segmentation from MRI, offering robust output against variations in threshold selection and pathology presentation.

Abbreviations: SOTA:, state-of-the-art; MRI:, magnetic resonance imaging; nPVS:, perivascular spaces.

* Correspondence to: Centre for Clinical Brain Sciences, Chancellor's Building, 49 Little France Crescent, Edinburgh EH16 4SB, UK.
E-mail address: M.Valdes-Hernan@ed.ac.uk (M.C. Valdés Hernández).

https://doi.org/10.1016/j.jneumeth.2023.110037
Received 30 September 2023; Received in revised form 6 December 2023; Accepted 17 December 2023
Available online 26 December 2023

Table 1
Overview of the performance, application in datasets different from the one(s) used for their development, and code availability, of the fully automatic PVS segmentation methods* published up to September 2023 and indexed in Web of Science.

Method	Relevant references	Performance in the validation dataset (s) (mean values in testing / validation sample)	Application in other datasets	Availability for independent evaluation
Stochastic modelling of PVS geometry	Kruggel et al. (2002); Descombes et al. (2004)	Correlation with visual scores 0.77, ICC with one expert 0.87. Type I error (false positives) 13% and type II error (false negatives) 2.7%	Not found	Not found
Conventional techniques: thresholding, image gradients, or morphology analysis	Niazi et al. (2018); Schwartz et al. (2019); Boespflug et al. (2018)	0.77% false positive and 19.39% false negative pixels compared against visual counting; Correlations (with visual counting, and repeated measures in single slice and whole brain): $0.72 \leq r \leq 0.87$, and with visual rating scores: $0.58 \leq r \leq 0.69$	Veterans (n = 56;Piantino et al., 2021), older adults (n = 181;Vikner et al., 2022), patients with behavioural variant frontotemporal dementia (n = 10;Moses et al., 2022), astronauts (n = 11; Hupfeld et al., 2022)	Not found
Frangi vesselness filter followed by thresholding	Ballerini et al., (2016, 2018);Sepehrband et al. (2019)	Compared to visual scores: Lin's concordance coefficient 0.81, Pearson's correlation coefficient 0.61, Spearman's ρ correlation coefficient $0.57 \leq \rho \leq 0.75$	Older adults (n = 540;Valdés Hernández et al., 2020,Hamilton et al., 2021,Aribisala et al., 2023), epilepsy (n = 332;Liu et al., 2020), Human Connectome Project (n = 897;Barisano et al., 2021), AD patients (n = 596,Sepehrband et al., 2021)	Valdés Hernández et al. (2023)
Vesselness filter as input to a machine learning scheme	Choi et al. (2020);Zhang et al. (2017)	ICC 0.98 (validation set n = 10), DSC 0.66	Not found	https://github.com/hufsaim/pvsseg
Conventional machine learning (e.g., random forest, support vector machine)	Neural network:Uchiyama et al. (2008) Random forest:Park et al. (2016),Sudre et al. (2022) K-nearest neighbour classifier:Spijkerman et al. (2022)	AUC 0.945 to differentiate lacunar infarcts from PVS; $0.72 \leq DSC \leq 0.73$, Sensitivity 0.69, PPV 0.80; F1 38.92, AED 16, AVD 45.20	Not found	Not found
Deep learning	Sudre et al. (2022);Lian et al. (2018);van Wijnen et al. (2019);Boutinaud et al. (2021)	PPV 0.83, $0.53 \leq$ Sensitivity ≤ 0.74; $45.7\% \leq FAUC \leq 53.1\%$, $0 \leq F1 \leq 35.8$, $0.28 \leq DSC \leq 0.77$, $45 \leq AVD \leq 390$	Healthy adults (n = 161,Wang et al., 2021, Huang et al., 2021)	https://hub.docker.com/r/whereisvaldo/challenge2021/tags; https://github.com/pboutinaud/SHIVA_PVS

Legend: PVS: Perivascular Spaces, AUC: Area Under the (ROC) Curve, FAUC: F stat (ratio of two variances) of the AUC from two measurements (e.g. manual vs. automatic), ICC: Intra-class Correlation Coefficient, AVD: Absolute Volume Difference (mm^3), DSC: Dice Similarity Coefficient, PPV: Positive Predicted Value, AED: Absolute Error Distance
Note *this table excludes semi-automatic (e.g., GUI-based), quantification, and automatic scoring methods, and only references initial publications of the methods, not further variations, adaptations or improvements

1. Introduction

1.1. Perivascular spaces and their relevance

Perivascular spaces (PVS) are cerebrospinal or interstitial fluid-filled cavities surrounding perforating cerebral microvessels as they course from the subarachnoid space to the brain parenchyma (Wardlaw et al., 2020). They are part of a brain-wide system that facilitates waste elimination, interstitial fluid exchange, and the distribution of non-waste compounds, hence playing a crucial role in the maintenance of healthy brain function (Brown et al., 2018; Jessen et al., 2015; Mestre et al., 2017; Aribisala et al., 2023). Usually microscopic, PVS become visible on magnetic resonance imaging (MRI) when enlarged or dilated (Wardlaw et al., 2020). The burden of MRI-visible PVS has high heritability and genetic associations (Duperron et al., 2023), and has been associated with sleep disturbances (Aribisala et al., 2020), cerebrovascular diseases and risk factors (Liu et al., 2021), with recent studies showing these being largely location-dependant (Doubal et al., 2010; Francis et al., 2019; Potter et al., 2015b; Valdés Hernández et al., 2020). However, debates remain over whether these associations are accurate and significant or not, given the modest sample sizes of the majority of the individual studies (Francis et al., 2019; Wardlaw et al., 2020) and limitations in the MRI analysis methods that generate the PVS assessments (Pham et al., 2022; Moses et al., 2023).

1.2. Computational identification of PVS candidates

With little variation, despite the surge of deep learning methods and their application to PVS segmentation (Pham et al., 2022; Moses et al., 2023), the most widely applied state-of-the-art PVS segmentation methods rely on identifying and enhancing tubular-like structures, followed by thresholding the output of this filtering procedure (Table 1). Due to their characteristic contrast (i.e., hypointense in T1-weighted (T1W) and fluid-attenuated inversion recovery (FLAIR), and hyperintense in T2-weighted (T2W) MRI) and geometric properties (e.g., local curvature and eccentricity), determination of the position and orientation of PVS in MRI can be achieved using image gradients (Niazi et al., 2018), and morphology analyses (e.g., Ballerini et al., 2016, Boespflug et al., 2018, Schwartz et al., 2019), these commonly via eigen analysis of the Hessian matrix (Frangi et al., 1998; Lamy et al., 2021; Bernal et al., 2021). The Frangi filter, the Hessian-based vessel enhancement method most widely applied, analyses three eigenvalues of the Hessian matrix (denoted as α, β, and c), allowing 'blob-like', linear and low intensity structures to be filtered out (Frangi et al., 1998). For each given image, a vesselness likelihood response map is created. The final response can additionally be thresholded to further reduce false positives. New approaches towards vesselness filtering have also been suggested (Lamy et al., 2021, Bernal et al., 2022). Of particular interest is the Jerman filter, which aims to respond better to varying morphologies, contrasts and bifurcations (Jerman et al., 2016). Unlike the Frangi filter, it additionally normalises the eigenvalues of the Hessian matrix depending on

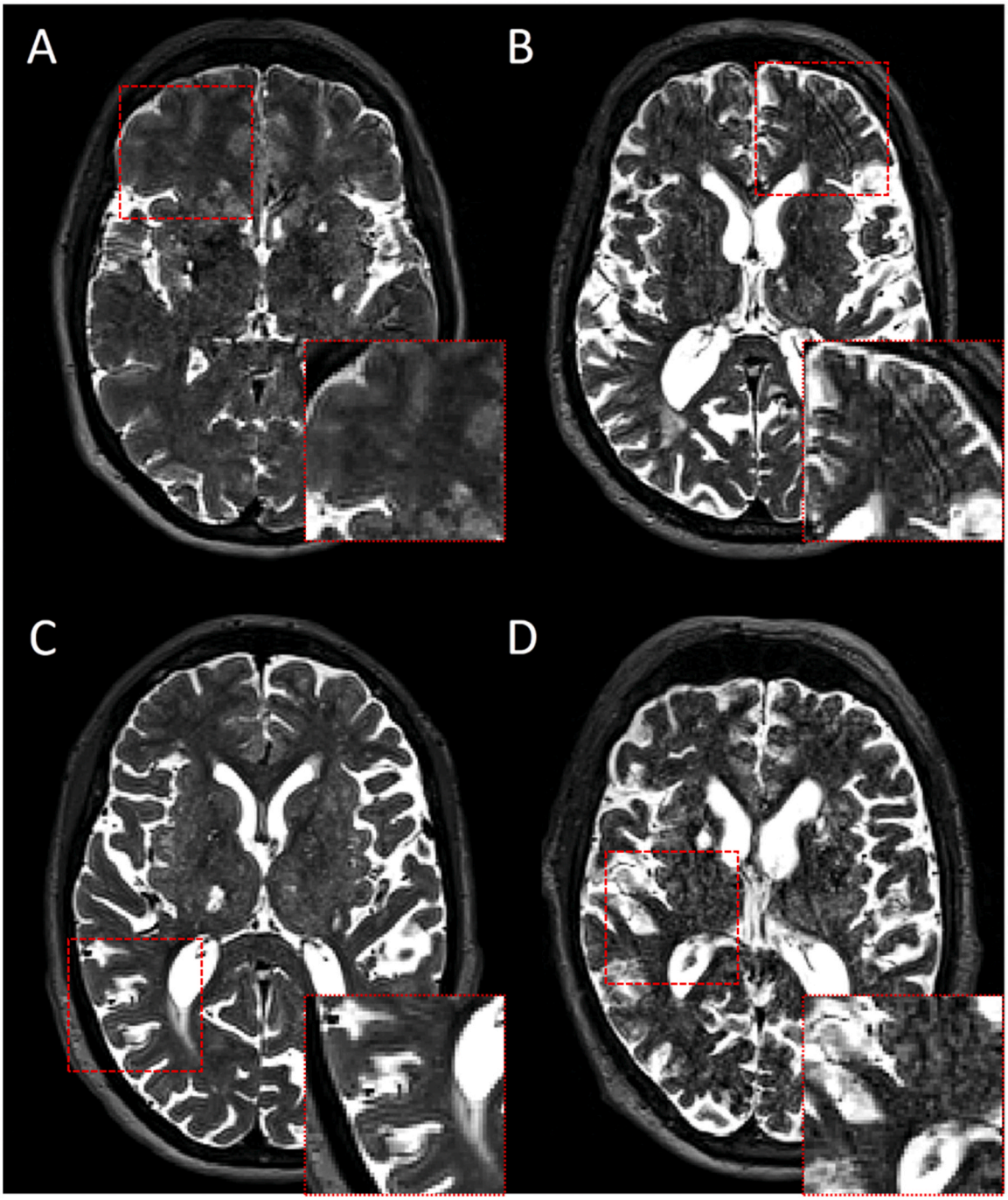

Fig. 1. Axial slices of T2-weighted MRI scans illustrating common imaging artefacts, indicated by red boxes. A: blurring; B: effect of motion artefact; C: ghosting effect around the sulci of the right parieto-occipital lobe and effect of truncation artefact; D: noise in the basal ganglia (mainly).

the relative brightness of the structures of interest compared to the surrounding background (Jerman et al., 2016). The vesselness likelihood response of the Jerman filter is controlled by a single parameter, which acts as a threshold for the filter's sensitivity to noise and low contrast structures (Jerman et al., 2016). Similarly, this response can also be thresholded by adjusting this parameter. The single parameter controlling the filter's vesselness likelihood response is particularly noteworthy, given that optimising a single parameter is a far more straightforward process than optimising the three parameters of the Frangi filter. Although the characteristics of this filter, therefore, may hold great potential, in-silico experiments did not show promising results comparatively in this specific application (i.e., PVS segmentation) (Bernal et al., 2022).

1.3. Confounders in the identification of enlarged perivascular spaces from MRI

Although computational segmentation techniques overcome the limitations of visual scores (Ballerini et al., 2020; Pham et al., 2022), they are still vulnerable to the presence of imaging artefacts and other disease-related imaging confounds (Bernal et al., 2022; Valdés Hernández et al., 2013), and can give inconsistent results depending on the robustness of the software implementation. Artefacts affecting PVS segmentations are caused by complex interactions between image structure, patient movement, sequence parameters and the k-space acquisition strategy, manifesting primarily as blurring (Fig. 1A), ringing (Fig. 1B) or ghosting (Fig. 1C) (Shaw et al., 2020; Wood and Henkelman,

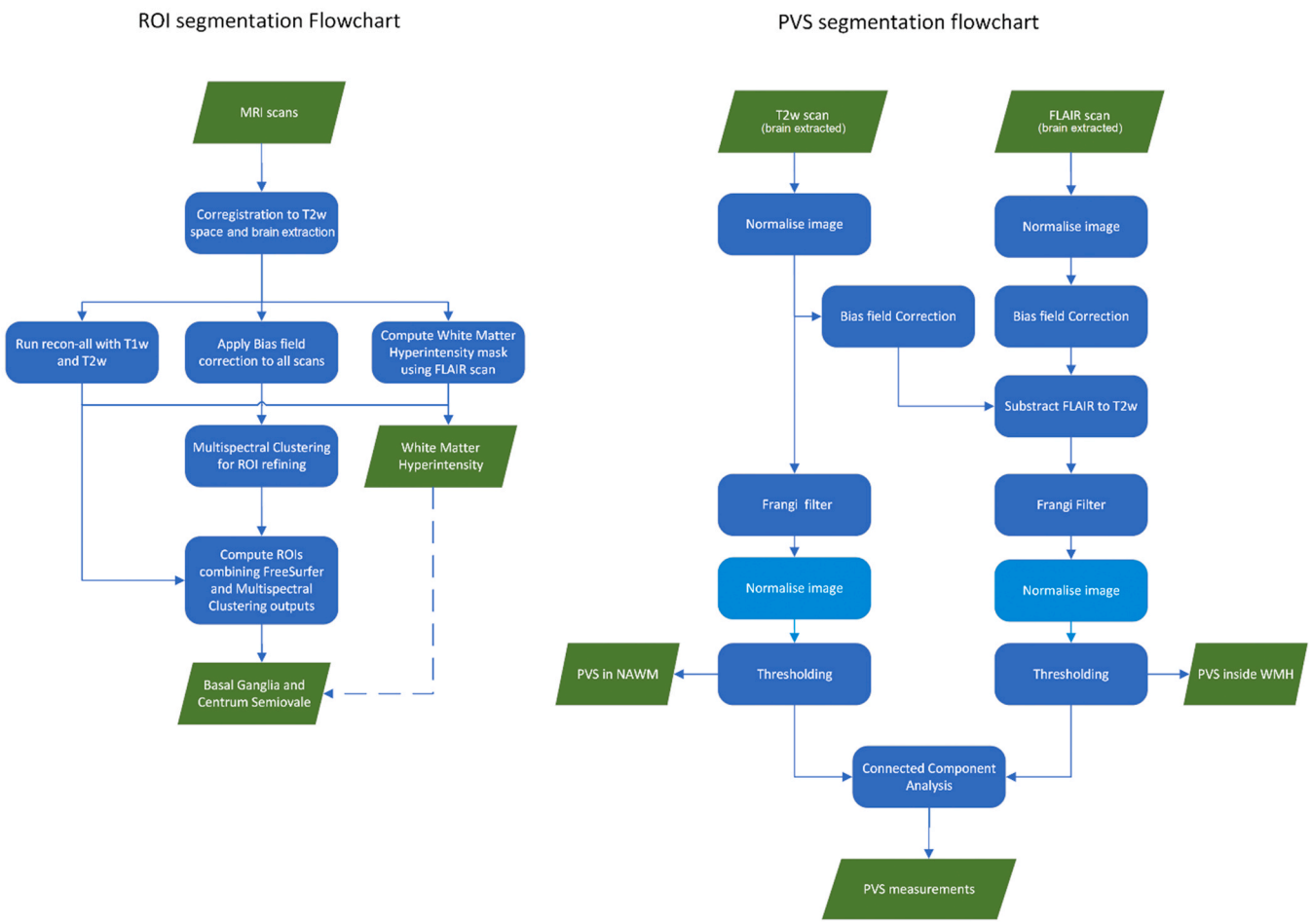

Fig. 2. Flow charts of the ROIs and PVS segmentations. This study evaluates the usefulness of the normalisation of the filter response (blocks highlighted in a different blue tone).

1985; Zaitsev et al., 2015). Separate to these are noise, discretisation or MR reconstruction artefacts (Fig. 1D) (McRobbie et al., 2006). Different pre-processing schemes have been proposed to limit the impact of the main sources of artefacts on the image quality (Godenschweger et al., 2016; Bernal et al., 2021). But these artefacts, although in levels that may deem the image quality as "acceptable", reduce the level of detail available while increasing the likelihood of false positives being detected (Bernal et al., 2020, 2021) altering PVS segmentation and, therefore, quantification up to levels which have not been so far documented for in-vivo MRI. Neither has the impact in clinical research of using different imaging sequences (i.e., T1-weighted vs. T2-weighted), or differences in the selection of what authors describe as "the optimum threshold" for segmenting filter's responses been documented.

1.4. Our aims, hypotheses and contributions

In-silico evaluation of the performance of different methods for facilitating the detection of PVS-like structures concluded that all the three filtering methods are heavily influenced by imaging quality, with sampling and motion artefacts being the most relevant (Bernal et al., 2022). The same study simulated the presence of other hyperintense structures (e.g. white matter hyperintensities (WMH), stroke lesions, or lacunes) and reported that none of the filtering methods evaluated could distinguish PVS-like structures from these simulated confounds. This study builds on these previous evaluations but using only the Hessian-based filters and brain images from in-vivo 3 T brain MRI of individuals with sporadic small vessel disease (i.e., with WMH, stroke lesions and lacunes as well as PVS) seeking to answer the following questions:

1) Do differences in selecting the threshold to the filter response impact the results? If so, how?
2) Do different strategies of intensity normalisation impact the results? If so, how?
3) Do differences in quantitative results from assessments using T1-weighted vs. T2-weighted impact the associations between PVS and age, vascular risk factors and WMH?
4) Can an image-quality-based threshold of the filter response help in the quantification of PVS?

We hypothesise that although all responses to the above questions will be affirmative, it is possible to minimise the impact of these potential sources of discrepancies in PVS identification, and that the information will guide choice of MRI sequence for analysis. We evaluate modifications of a state-of-the-art PVS segmentation method that uses Hessian-based filtering as a core element to detect PVS, to formulate recommendations.

2. Materials and methods

2.1. Sample

We utilised brain MRI, clinical and demographic data obtained at the baseline scan from patients who presented to clinics in the Scottish region of Edinburgh/Lothians with mild stroke symptoms (modified Rankin scale (mRS) ≤ 2) between August 2018 and November 2021,

Table 2
Sample clinical and demographic characteristics (n = 228).

Parameter		Value
Age (mean (SD))		65.77 (11.17)
Sex (F/M)		78 (34%)/152 (66%)
Diabetes (n (%))		50 (22)
Hypertension (n (%))		157 (69)
Hypercholesterolaemia (n (%))		171 (75)
Smoking status	Never (n (%))	99 (43)
	Current (n (%))	29 (13)
	Ex-smoker > 1 year (n (%))	86 (38)
	Ex-smoker < 1 year (n (%))	12 (5)
PVS scores (0 – 3)	CSO (median [IQR])	2 [2 3]
	BG (median [IQR])	2 [1 2.25]
Fazekas WMH scores	Periventricular (0 - 3)(median [IQR])	1 [1 2]
	Deep (0 – 3)(median [IQR])	1 [1 2]
	Total (0 – 6)(median [IQR])	3 [2 4]
Lacunes	≥ 1 lacune (n (%))	120 (53)
	≥ 3 lacunes (n (%))	59 (26)
Brain Microbleeds (BMBs)	≥ 1 BMB (n (%))	43 (19)
	≥ 3 BMBs (n (%))	21 (9)

Table 3
PVS measurements per threshold selection and T2W image normalisation schemes (n = 110). The symbols (s), ˆ, and * indicate group measurements that do not statistically differ.

Measurements	Whole-brain intensity normalisation pre-filtering. Unique threshold (Scheme 1)		Intensity normalisation of post-filtered ROIs. Thresholds per ROI (Scheme 2)	
	Threshold 1	Threshold 2	Threshold 1	Threshold 2
Centrum semiovale (CSO)				
CSO PVS count (median [IQR])	921 [720.75 1119.5] (s) *	659.5 [482.5 901]	990 [787 1195] (s)	839.5 [608 1087] *
CSO PVS volume (ml, mean (SD))	12.64 (6.75) (s)	7.80 (5.09)	13.86 (7.22) (s)	10.10 (6.04)
CSO PVS average length (mm) (median [IQR])	3.72 [3.53 3.99] (s)	3.96 [3.68 4.22] *	3.68 [3.51 4.01] (s)	3.85 [3.67 4.14] *
CSO PVS average width (mm) (median [IQR])	1.99 [1.94 2.01] (s)	1.99 [1.95 2.03] (s) *	1.97 [1.93 2.00] (s) ˆ	1.99 [1.95 2.02] (s) * ˆ
Basal ganglia (BG)				
BG PVS count (median [IQR])	201 [177.25 218.75]	183 [163.25 207]	158 [140.25 187] (s)	169.5 [149.5 197] (s)
BG PVS volume (ml, mean (SD))	5.33 (1.33)	3.64 (1.15)	2.52 (1.01) (s)	2.79 (1.06) (s)
BG PVS average length (mm) (median [IQR])	3.14 [3.06 3.31]	3.39 [3.27 3.53]	3.50 [3.40 3.68] (s)	3.47 [3.34 3.60] (s)
BG PVS average width (mm) (median [IQR])	1.84 [1.75 1.93]	1.96 [1.88 2.01] *	2.00 [1.96 2.05] (s)	1.98 [1.93 2.03] (s) *

who enrolled in a prospective observational longitudinal study of small vessel disease: the Mild Stroke Study 3 (MSS3, registered ISRCTN 12113543) (Clancy et al., 2021). The MSS3 was approved by the South East Scotland Research Ethics Committee (Ref 18/SS/0044) and by the NHS Lothian Research & Development (Ref 2018/0084), on 31 May 2018. Participants attended their baseline MRI scan, on which the present cross-sectional analysis is based, within 3 months of acute stroke presentation. We used these data since the study is large, clinically relevant to the study of small vessel disease, and provides 3D T1-weighted and 3D T2-weighted images with high spatial resolution on which to evaluate the PVS processing methods in the same patients and at the same scanning session.

The full image acquisition protocol of the study is published in Clancy et al. (2021). Of note, 3D T1-weighted (T1W) images were acquired with TR/TE/TI = 2500/4.37/1100 ms and 7° flip angle, and have isotropic 1 mm^3 voxels; 3D T2-weighted (T2W) images were acquired with TR/TE = 3200/408 ms, and had voxel size of dimensions 0.90 mm × 0.937 mm× 0.937 mm. The demographic variables used in this study are age at presentation and gender assigned at birth. The clinical variables used are vascular risk factors (i.e., diabetes (yes/no), hypertension (yes/no), hypercholesterolaemia (yes/no), current or recent smoker (yes/no)), WMH Fazekas scores (Fazekas et al., 1987), and PVS visual rating scores as per Potter et al. (2015a).

2.2. Image processing

2.2.1. PVS segmentation

PVS were assessed in the basal ganglia (BG) and centrum semiovale (CSO) regions (ROIs) separately and independently on T1W and T2W images from all patients. The ROIs in which the PVS were measured were generated by combining the brain parcellation output from Freesurfer™ 6.0, with the probabilistic masks of cerebrospinal fluid and pial/meningeal layers obtained from a multispectral Gaussian clustering that used T1W, T2W and FLAIR images simultaneously, all in the T2W native image space. For segmenting PVS on the T1W images, all PVS ROIs were registered to the native T1W image space afterwards using rigid body registration and nearest neighbour interpolation. All co-registrations used niftyreg (http://sourceforge.net/projects/niftyreg/), which was called through TractoR (http://www.tractor-mri.org.uk/diffusion-processing). Stroke lesions were manually delineated, and WMH were segmented semi-automatically (see Clancy et al., 2021 supplementary materials) and were excluded from the ROIs for these analyses. PVS segmentation masks were generated by thresholding the output from the vesselness filters applied to brain-extracted images. We used the recommended filter parameters: $\alpha = 0.5$, $\beta = 0.5$, and c= 500 for Frangi (Ballerini et al., 2018), and $\tau = 0.5$ for Jerman (Jerman et al., 2016) to enhance the tubular structures (i.e., PVS), as opposed to wedge-shaped or irregular-shaped structures (i.e., lacunes, white matter hyperintensities and other ischaemic lesions). Further differentiation between elongated lacunes and clustered PVS was achieved by applying the k-means clustering to areas corresponding to large connected components, which separated the PVS that were close to each other and previously considered a single "object". PVS count was defined as the number of connected components in each ROI. The PVS segmentations performed on T2W images were considered the reference segmentations (i.e., over those performed on T1W), as the updated Standards for Reporting Vascular Changes on Neuroimaging (STRIVE) criteria (Duering et al., 2023) recommends. Fig. 2 shows a flow chart of the ROIs and PVS segmentations. The full step-by-step image processing pipeline can be found in Valdés Herrnández et al. (2023), downloadable from https://doi.org/10.7488/ds/7486.

2.2.2. Influence of threshold and normalisation strategy

From the first 122 patients imaged, we used clinical and imaging data from the 110 patients with T2W images considered of enough quality, and evaluated two PVS segmentation schemes. The first (i.e., Scheme 1) consisted in linearly normalising the image intensities of the whole brain-extracted T2W image to values in the range from 0 to 255 prior to applying the vesselness filter, and converting into a logarithmic scale the filtered result for enhancing intensity differences, therefore, facilitating the selection of a unique threshold across the image (i.e., as opposed to selecting a threshold per ROI). The second scheme (i.e., Scheme 2) applied first the vesselness filter and, then, linearly normalised the intensities of the filtered image separately in BG and CSO ROIs, also in the range from 0 to 255. Two different observers, independently, arrived at two different threshold combinations (i.e., separately for BG and CSO). Two different thresholds, also independently selected, were also evaluated in Scheme 1.

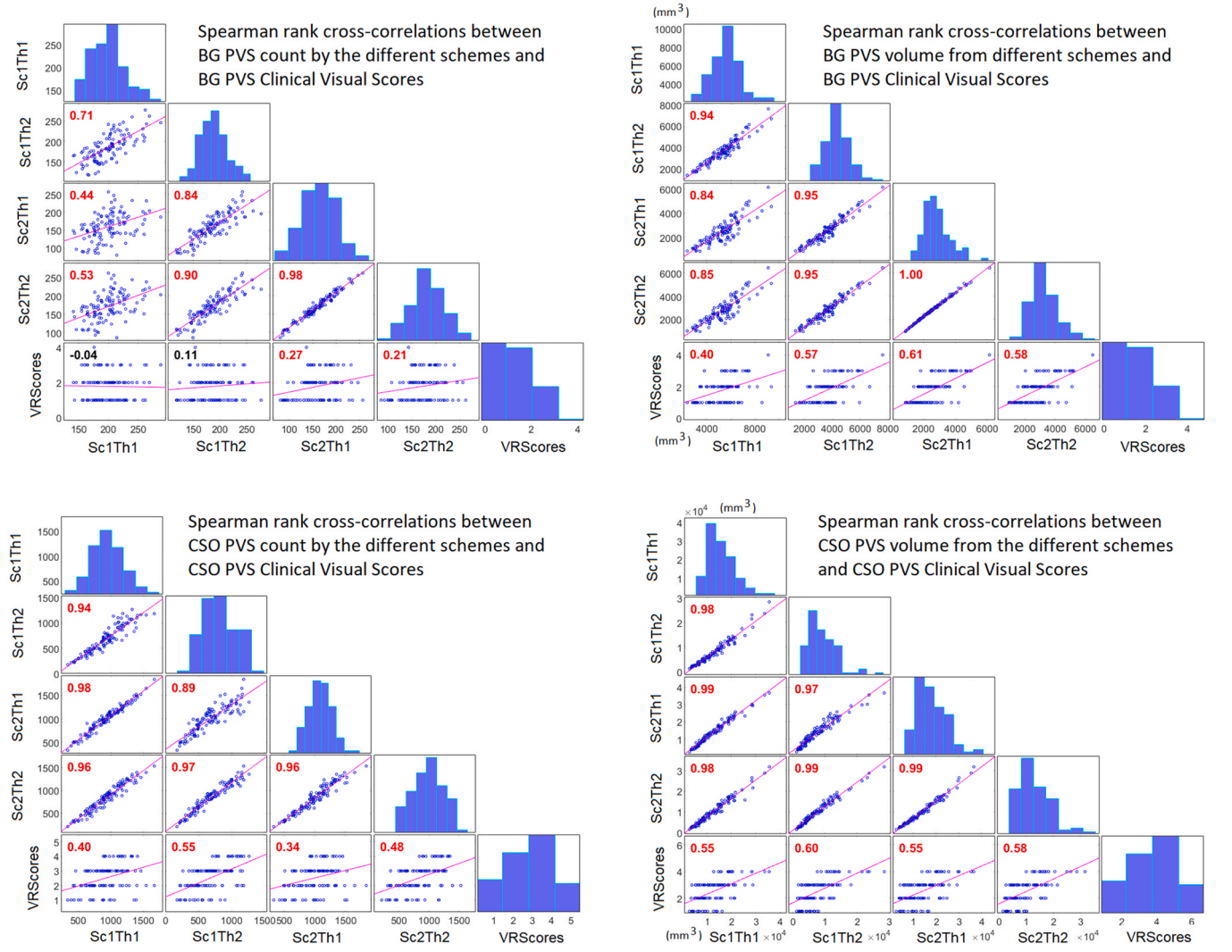

Fig. 3. Spearman rank cross-correlations between PVS count and volume in BG and CSO from the schemes evaluated to assess influence of normalisation procedure and inter-observer differences in threshold selection, and visual rating (VR) scores (n = 110). Sc1 refers to the scheme 1 where the overall brain intensities were normalised prior to filtering and a single threshold was used for BG and CSO, Sc2 refers to the scheme 2, where intensities were normalised separately in BG and CSO after applying the Frangi filter and different thresholds were selected for BG and CSO. Th1 and Th2 refer to the two different thresholds selected independently in both schemes.

2.2.3. *Influence of noise and artefacts*

In a subsample of 60 patients, selected to ensure all T2W images with artefacts were included, we analysed the influence of noise and artefacts in measurements using the Jerman filter vs. the Frangi filter for PVS enhancement. We segmented the PVS using the Scheme 2. To determine the optimum threshold one observer selected an initial threshold, based on previous evaluations and recommended values (Ballerini et al., 2018), and systematically varied it in steps of ± 0.01 until the result was visually acceptable. Image quality was assessed computationally as per Bernal et al. (2021) using mriqc (https://mriqc.readthedocs.io/en/latest/), and validated against neuroradiological scores generated blind to the computational results. The metrics used to evaluate the image quality and considerations on their appropriateness are summarised in the Supplementary material (file Supplementary_material_2_Image_quality_assessment.pdf). For these analyses and threshold optimisation, the T2W images in this subset were classed as "clean" and "noisy" depending on the presence of the imaging artefacts mentioned and illustrated previously, visually identified, and guided by the results from mriqc.

2.2.4. *Use of T1-weighted vs. T2-weighted sequences*

This evaluation uses data from 217 out from the 228 patients that comprise the total sample, as images from 11 patients had excessive noise and were discarded. We calculated density of PVS per ROI defined as the number of PVS identified per ml in each ROI, and percentage of PVS volume in each ROI using the PVS segmentation results from T1W and T2W, for a fair comparative analysis (i.e., given that the ROI volumes might have changed slightly in the registration process). We evaluated the impact of excluding (vs. not) PVS in the WMH. In T2W, PVS in the WMH were segmented as described in Barnes et al. (2022). Briefly, we used the same method described above (i.e., thresholding the output of the 3D Frangi filter) but using an image obtained by subtracting the FLAIR MRI sequence from the T2W after applying bias-field correction using FSL-FAST (Zhang et al., 2001) and intensity normalisation. For obtaining the PVS in WMH on T1W, we only removed the stroke lesions from the PVS ROIs. All segmentation results were visually checked independently in T1W and T2W, and corrected for errors that could be derived from the image processing: white/grey matter boundaries and ventricular edges that could be mistaken by PVS due to imprecisions in the co-registration of the ROIs.

Table 4
Results from exploring known associations between PVS and age, PVS and hypertension, and PVS and WMH for each scheme and threshold (adjusting also for sex, high cholesterol and smoking) (n = 110).

Param.	Scheme	Age			Hypertension			WMH (total Fazekas)		
		B	SE	p- value	B	SE	p-value	B	SE	p-value
BG	Sc1Th1	-0.75	0.29	0.011	-2.10	6.58	0.75	0.61	2.34	0.79
PVS	Sc1Th2	0.33	0.33	0.33	11.21	7.62	0.14	3.42	2.71	0.21
count	**Sc2Th1**	**0.89**	**0.36**	**0.014**	**21.80**	**8.07**	**0.008**	3.22	2.87	0.26
	Sc2Th2	**0.76**	**0.36**	**0.036**	**20.56**	**8.08**	**0.012**	2.30	2.88	0.43
BG PVS vol. (mm^3)	**Sc1Th1**	**31.42**	**12.39**	**0.013**	**653.36**	**279.87**	**0.021**	135.26	99.63	0.18
	Sc1Th2	**31.90**	**10.35**	**0.0026**	**549.92**	**233.77**	**0.020**	**178.36**	**83.22**	**0.034**
	Sc2Th1	**27.80**	**9.21**	**0.0032**	**464.76**	**208**	**0.028**	**158.01**	**74.05**	**0.035**
	Sc2Th2	**29.32**	**9.62**	**0.0029**	**498.15**	**217.26**	**0.024**	**159.99**	**77.34**	**0.041**
CSO PVS count	**Sc1Th1**	**9.71**	**2.55**	**0.0002**	121.27	57.72	0.038	10.88	20.55	0.60
	Sc1Th2	**10.17**	**2.53**	**0.0001**	112.54	57.25	0.052	6.07	20.38	0.77
	Sc2Th1	**9.99**	**2.78**	**0.0005**	109.03	62.80	0.085	-2.58	22.36	0.91
	Sc2Th2	**10.8**	**2.85**	**0.0002**	115.64	64.30	0.075	3.24	22.89	0.89
CSO PVS vol. (mm^3)	**Sc1Th1**	**230.08**	**66.37**	**0.0008**	2089.6	1499	0.17	-449.4	533.64	0.40
	Sc1Th2	**151.7**	**51.12**	**0.0037**	1283.8	1154.4	0.27	-289.7	410.96	0.48
	Sc2Th1	**243.15**	**71.46**	**0.0009**	1845	1613.9	0.25	-376.9	574.54	0.51
	Sc2Th2	**186.76**	**60.45**	**0.0026**	1353.1	1365.2	0.32	-235.5	486.01	0.63

Note: Sc1 refers to the scheme 1 where the overall brain intensities were normalised prior to filtering and a single threshold was used for BG and CSO, Sc2 refers to the scheme 2, where intensities were normalised separately in BG and CSO after applying the Frangi filter and different thresholds were selected for BG and CSO. Th1 and Th2 refer to the two different thresholds selected independently in both schemes.

2.3. Statistical analysis

Statistical analysis was performed in Matlab R2019b and R (version 3.6.2). We compared the influence of threshold and normalisation strategy in the 4 groups of measurements using the Kruskal-Wallis test. We compared the measurements using T1W vs. T2W using the Wilcoxon rank sign test. We used the Spearman rank correlations to compare clinical PVS scores and computational counts and volumes. To explore interchangeability in the use of each scheme/base image for clinical research purposes, we evaluated known associations between the PVS measurements and age, hypertension, and WMH (Wardlaw et al., 2020), in multivariable linear regression models where the outcome variable was the PVS measurement, and the predictors were: age, hypertension, and total Fazekas scores, adjusting also for sex, hypercholesterolaemia, and smoking. To explore the extent into which number of lacunes, cerebral microbleeds, and WMH influence the T1W measurements, we used ANCOVA models (T1W_PVS parameter ~ b1 * T2W_PVS parameter + b2 * no. microbleeds + b3 * no. lacunes + b4 * total Fazekas).

For evaluating the influence of noise and filtering approaches we separately represented the distribution of the PVS counts for noisy and "clean" scans to also assert sensitivity vs. robustness of the threshold selection and filtering approaches to imaging artefacts deemed suitable for neuroradiological (i.e. visual clinical) assessments. We also calculated the correlation between regional PVS counts from the tested scenarios in the subsample (n = 60) and visual rating scores, and visually assessed the quality of the segmentations.

3. Results

3.1. Sample characteristics

From the 229 patients recruited, we analysed image data from 228 (1 claustrophobic) (Table 2). T2W images from 18 patients were corrupted by artefacts, of which six were mild and were considered not to affect the PVS measurements.

3.2. Influence of threshold and normalisation strategy

Table 3 shows the median and interquartile range [QR1 QR3] from the two schemes evaluated, and the results from the multiple comparison group tests. In the BG, normalising the overall brain intensities pre-filtering and using a single threshold for BG and CSO ROIs (Scheme 1) produced statistically significantly different measurements for each threshold, which also differed from those obtained from normalising the post-filtered intensities separately in the BG from the CSO (Scheme 2). Inter-observer differences in selecting the threshold for segmenting PVS in the BG using the Scheme 2 did not affect the results. In the CSO, the pattern of group measurement differences was more heterogeneous, although for one of the thresholds selected for both schemes, PVS measurements in the CSO from one scheme were not different from the other. The PVS individual measurements (e.g. width and length) in the CSO seem to be quite insensitive to threshold selection and image normalisation methods (See differences between estimated group means, 95% confidence intervals and p-values in Supplementary Table 1, and distribution of the measurements in Supplementary Fig. S1).

The PVS count and volumes were correlated among themselves and with the clinical visual rating scores (Fig. 3), with the exception of the BG PVS count produced by Scheme 1. Inter-observer differences in threshold selection in Scheme 2 did not affect the correlations.

Table 4 shows the results from the multivariable linear regression models. Hypertension, increasing age, and high burden of WMH (i.e., higher total Fazekas scores) were associated with the BG PVS count and volume assessed using Scheme 2. The BG PVS volume from Scheme 1 was only associated with age and hypertension. In the CSO, PVS count and volume from both schemes, regardless differences in thresholds, were consistently associated with age. CSO PVS count from Scheme 1, additionally, had a borderline association with hypertension.

3.3. Influence of noise and artefacts

The PVS burden and image quality distribution in the subsample of 60 patients used for this analysis mirrors those of the whole sample (Supplementary Fig. S2). The optimised thresholds for the images classed as "noisy", as expected, were higher than those considered optimal for the "clean" images, but in different proportions for each region and depending on the vesselness filter used. When using the Frangi filter, for the BG the optimum threshold for "noisy" images was 0.04 units higher than those for the "clean" images, and for the CSO 0.12 units. When using the Jerman filter, for the BG it was 0.01 units higher and for the CSO 0.02 units.

The distribution of PVS count for "clean" and "noisy" images using optimised vs. non-optimised thresholds can be seen in Fig. 4. In the clean scans, the median values and distributions of PVS count were similar for all schemes for both BG and CSO regardless of the filter and inter-

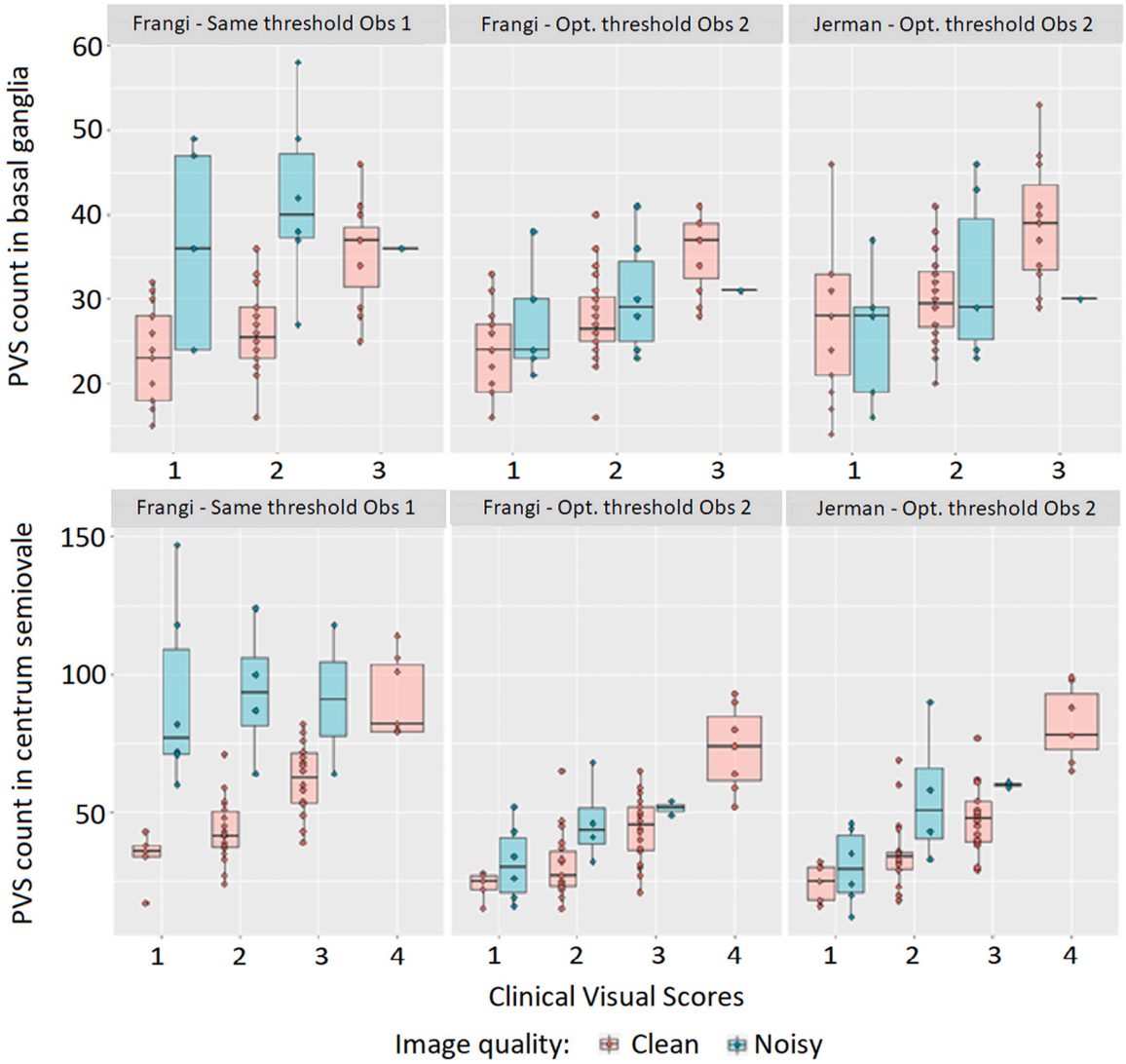

Fig. 4. Boxplots of PVS counts in the basal ganglia (above) and centrum semiovale (below) obtained using the same thresholds for noisy and clean images, and thresholds separately optimised for clean (pink) and noisy (turquoise) T2W images, after applying the Frangi and Jerman filters. Obs 1 and Obs 2 refer to the observers who selected the thresholds.

observer differences in thresholds. The PVS regional counts and visual rating scores were poorly correlated when the same thresholds were used for "clean" and "noisy" images (Spearman = 0.38 for BG), as opposed to when the thresholds were selectively optimised considering image quality (Spearman = 0.65 for BG using Frangi, and 0.58 for BG using Jerman). In the CSO, not using different thresholds for "noisy" and "clean" images yielded absence of correlation, contrasting with correlation values of 0.73 and 0.77 from thresholding the Frangi and Jerman filters' results respectively using the optimised values,.

Careful visual analysis of the PVS masks generated allowed us to identify three main inter-filter differences and filter-specific error patterns in the segmentation. The Frangi filter often segmented larger PVS clusters compared to the Jerman filter. Also, the Frangi filter outperformed the Jerman filter at discerning low intensity PVS. The Jerman filter particularly struggled in areas of high PVS burden, more so than the Frangi filter.

3.4. Use of T1-weighted vs. T2-weighted sequences

For this analysis, for a fair comparison, data from 11 patients were not used due to excessive noise either in T1W or T2W sequences. Measurements from T2W images statistically differed from those from T1W (Supplementary Table 2). Figs. 5 and 6 show the correspondence between PVS density (counts/ml) and volumes measured using T1W images with respect to the same measurements but obtained from T2W images a) considering only the PVS in the NAWM (panels A and B) and b) considering all PVS (panels C and D). T2W images allow detection of, on average, 1 PVS more per ml than T1W (Fig. 6), increasing proportionally with the number of PVS detected (Figs. 5 and 6). This pattern is consistent and almost identical for PVS counted in BG and CSO (mean (SD) density in T2W = 2.81(0.72) PVS/ml for BG and 2.75(1.02) PVS/ml for CSO, while mean density in T1W = 1.96(0.25) PVS/ml for BG and 1.80(0.37) PVS/ml for CSO), and PVS volumes in the CSO (mean (SD) PVS volume in T2W = 3.91(2.50) % in the CSO ROI, vs. mean PVS volume in T1W = 3.00(1.12) % in the CSO ROI) However, total PVS volumes in the BG measured in T1W are on average higher than the volumes reported for PVS segmented on T2W (Figs. 5 and 6, mean (SD) PVS volume in T2W = 4.93(2.27) % in the BG ROI, vs. mean PVS volume in T1W = 5.85(1.66) % in the BG ROI). Results were consistent regardless of whether PVS in WMH were included or not in the analyses.

Volumetric correspondence of PVS assessed on T2W with PVS volumes assessed on T1W excluding PVS in WMH (B) and including PVS in WMH (D). NAWM: normal-appearing white matter. Equations described linear tendencies and R^2 values are given for each analysis in BG

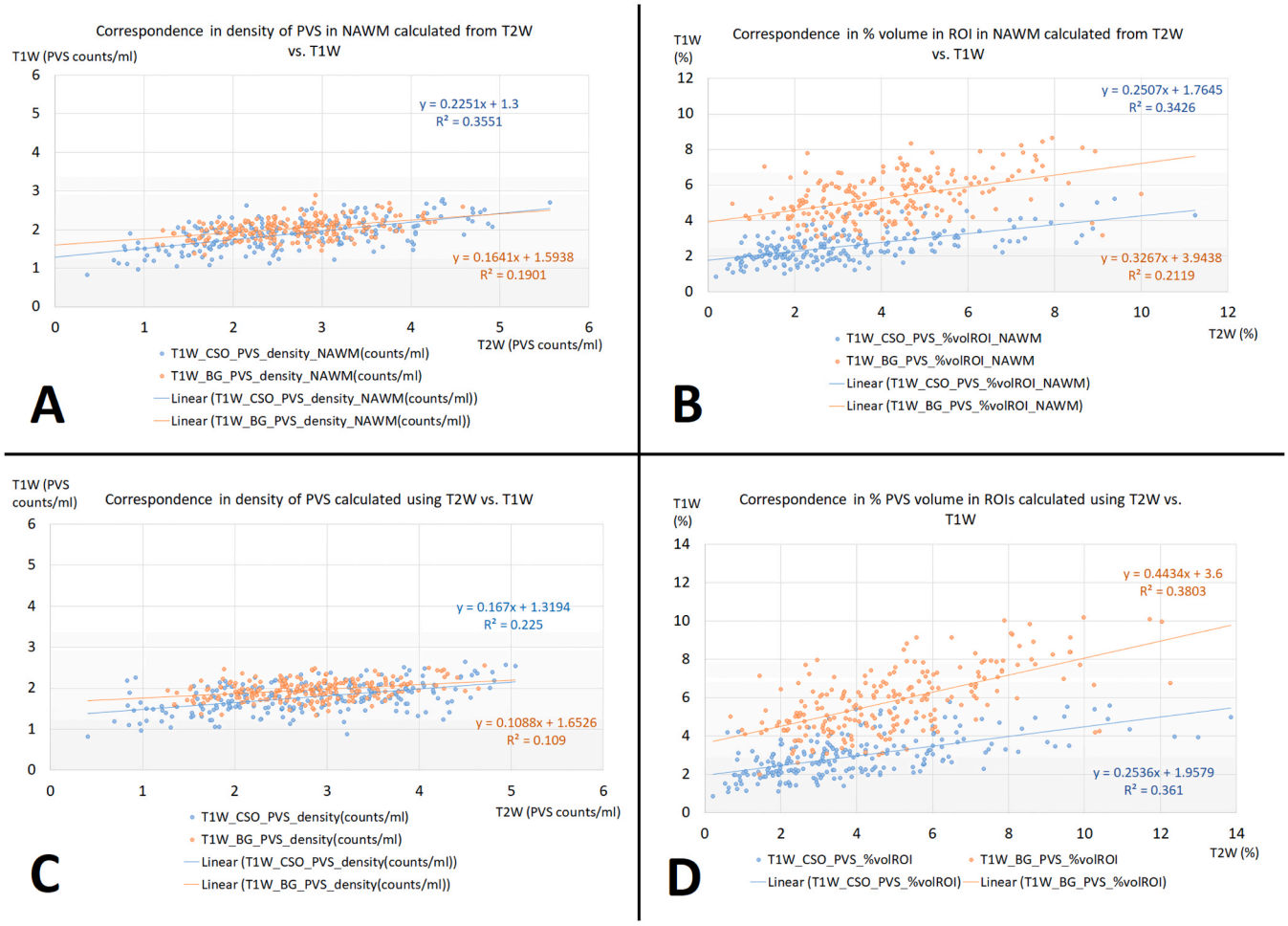

Fig. 5. Correspondence between regional density of PVS counted on T2W and regional density when PVS are counted on T1W excluding PVS in WMH (A) and including PVS in WMH (C).

(orange) and CSO (blue).

Visual inspection of the results shows large clusters of mineral deposits and calcified vessels in the BG being mistakenly segmented as PVS when T1W images are used (Fig. 7), which is not a problem when T2W images are used. Bland-Altman analyses of average PVS lengths and widths numerically corroborates this finding (Supplementary Fig. S3). ANCOVA models exploring the effect of cerebral microbleeds, lacunes, and WMH in PVS measurements on T1W (Supplementary Table 3) confirmed the effect of WMH in the PVS volumes in the BG (B=0.19%, SE=0.065%, $p = 0.0032$) and CSO (B=0.18%, SE=0.042%, $p < 0.0001$), and in the PVS counts in the CSO (B=−0.034 counts/ml, SE=0.016 counts/ml, $p = 0.034$), and the effect of lacunes in the PVS volumes in the BG (B=0.13%, SE=0.038, $p = 0.0012$).

Fig. 8 shows the correlation between visual scores and PVS measurements from T1W and T2W images. While visual scores highly correlated with PVS volumes assessed from both T1W and T2W images, they did not correlate with PVS counted in the BG when these were assessed from T1W images (Fig. 8A). Histograms of visual scores were more similar to those from computational measurements from T1W and T2W in the CSO (Figs. 8B and D) than in the BG (Figs. 8A and C).

The well-known associations between PVS burden and age, hypertension and WMH were reproduced only using the measurements from T2W images. Measurements from T1W yielded inconsistent results (Table 5).

4. Discussion

The present study uses structural MRI from patients with small vessel disease, known to be associated with PVS burden (Francis et al., 2019), and characterised by the coexistence of several features that can confound the computational assessment of PVS (Wardlaw et al., 2013), to evaluate the robustness and accuracy of a state-of-the-art PVS segmentation scheme that uses a Hessian-based filter to enhance vessel-like structures.

4.1. Influence of threshold and normalisation strategy

Our results indicate that the PVS segmentation method evaluated is relatively insensitive to normalisation strategies, and to inter-observer differences in selecting the threshold to be applied to the response of the vesselness filter. However, BG and CSO ROIs require different thresholds, which need to be independently and carefully selected. It must be pointed out that the evaluation of the threshold selection used only T2-weighted images. Sepherband et al. (2019) proposed to combine T2W with T1W images in an approach that pre-filters these images using an adaptive non-local mean technique to precisely increase robustness against noise, and enhance PVS vs. background contrast prior to applying the Frangi filter. Barnes et al. (2022) segment PVS within white matter hyperintensities using a combination of T2W and FLAIR images after both being corrected for bias-field inhomogeneities and their intensities being normalised, also to enhance filter response. Thus, the results presented here, instead of raising questions about their

Fig. 6. Bland-Altman plots of the agreement between regional densities of PVS counted on T2W and. PVS counted on T1W excluding PVS in white matter hyperintensities (A) and including them (C). Bland-Altman plots of the volumetric agreement between PVS assessed on T2W and PVS assessed on T1W excluding PVS in white matter hyperintensities (B) and including them (D). NAWM: normal-appearing white matter. Equations described linear tendencies, and mean differences between measurements with confidence intervals are given for each analysis in BG (orange) and CSO (blue).

applicability when these other multi-sequence approaches are used, reinforce the confidence in the approach that thresholds the Frangi filter output for segmenting PVS. Ultimately, the threshold selection always will be influenced by the contrast between foreground (i.e., enhanced tubular structures, likely to be PVS) and background (normal or abnormal brain tissue): the higher the contrast, the wider the range of suitable thresholds.

Our approach of systematic visual optimisation of the threshold to increase the fidelity in the PVS segmentation in absence of visual scores is unique, given the usual standard of mathematical and computational approaches for optimising filter responses (Ballerini et al., 2018; Choi et al., 2020; Zhang et al., 2017). Although it is limited by its time-consuming nature and the likelihood of intra-observer variability, its primary advantage relies in the results systematically achieved, which allow further experimental validation.

4.2. *Influence of noise and artefacts*

It is known that the presence of pathologies and imaging artefacts greatly influences the image contrast and therefore the optimum threshold for the task at hand. Previous attempts at improving PVS segmentation have mainly focused on either optimising filter parameters (Ballerini et al., 2016; Ballerini et al., 2018), or the acquisition quality in both pre- (Bernal et al., 2020; Bernal et al., 2021) and post-processing phases (Sepehrband et al., 2019). While these studies have considered the burden of pathology for optimising the PVS segmentation protocols, and some have proposed solutions to increase image quality, practical solutions to segment PVS in noisy images have not been proposed. Our analyses suggest the appropriateness of first classifying the scans in noisy and clean prior to PVS segmentation, and, afterwards, optimise vesselness likelihood thresholds in noisy and clean scans separately.

The fact that the Frangi filter often segments a larger region as PVS compared to the Jerman filter presents an interesting conundrum when determining the more suitable filter. While this does occasionally result in nearby PVS being incorrectly combined, it also conversely reduces fragmentation, a much greater problem. This would also provide more accurate measures of PVS volume, another variable that is currently of great interest and is being investigated for its clinical associations (Ballerini et al., 2020). The difficulties the Jerman filter faces segmenting low-intensity PVS and PVS of a high burden is unsurprising, given its approach of normalising the vesselness response in a ROI according to its maximum value. Therefore, if this maximum value is particularly greater than the mean (for example in areas of high PVS burden), many low contrast structures will not be detected. This problem is also compounded by the, very small and few but nevertheless existent, flaws in ROI masking, as incorrectly segmented PVS in ventricle borders and sulci have a much greater vesselness response than true PVS due to their particularly high intensity and contrast, skewing the maximum vesselness response and therefore increasing the contrast

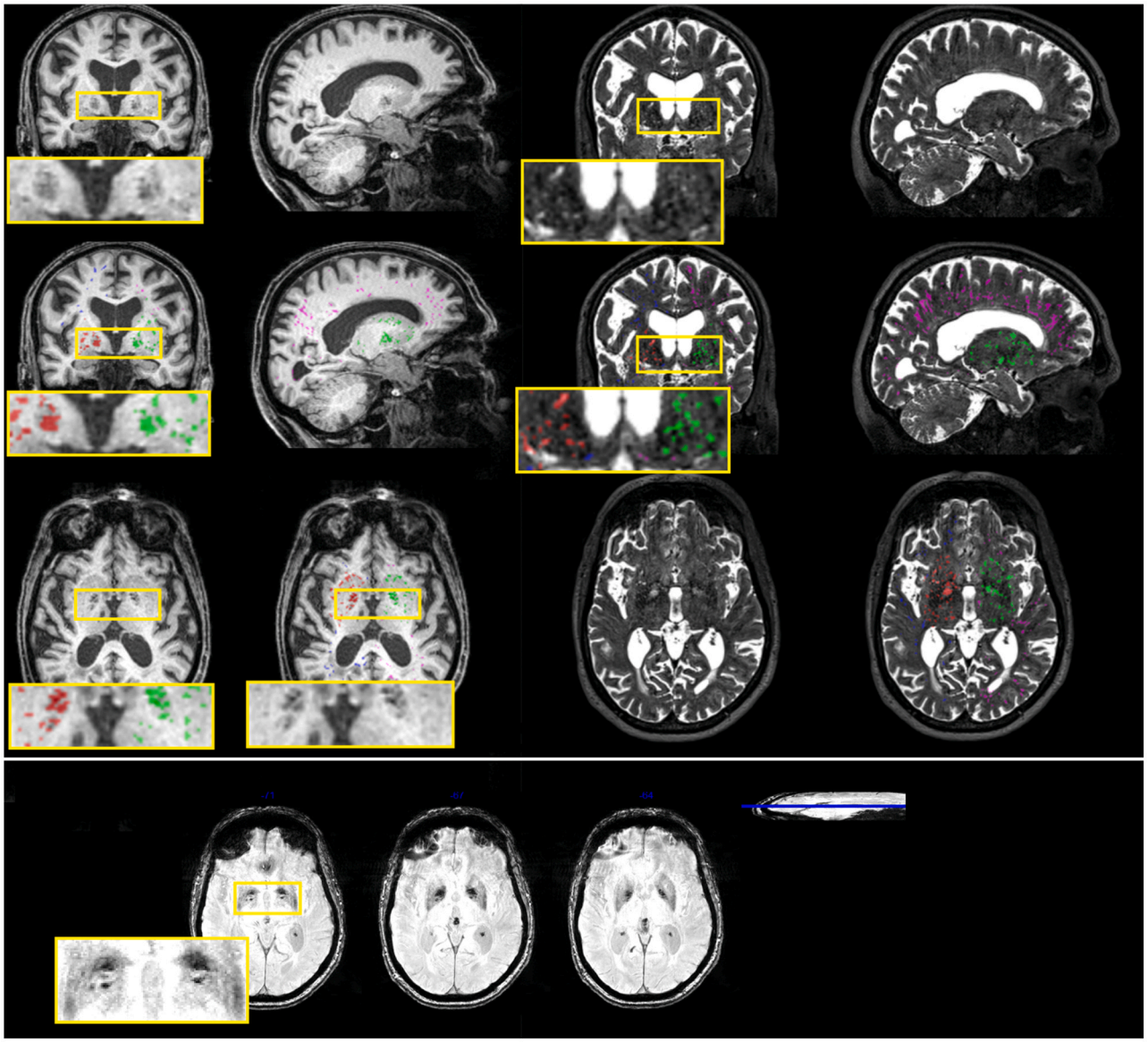

Fig. 7. Example of PVS segmentation results on T1W and the correspondent T2W images with insets highlighting confounding areas with calcifications in the basal ganglia. A coronal, sagittal and axial slices without and with the PVS segmentations overlaid on the correspondent sequence (green: left basal ganglia, red: right basal ganglia, indigo: right centrum semiovale, magenta: left centrum semiovale, in the panel above), and three consecutive axial slices of the susceptibility-weighted image from the same patient showing the mineralisation in the basal ganglia (panel below).

threshold at which structures are determined to be PVS. We also observed that vesselness likelihood thresholds of different filters are based on entirely different scales and have non-linear effects. During visual optimisation, the Jerman filter was found to be more sensitive to threshold adjustments than the Frangi filter. Future optimisations of the Jerman filter are therefore necessary to allow a fair judgement to be made.

4.3. Use of T1-weighted vs. T2-weighted sequences

In the sample analysed here, PVS assessment in T1W yielded surrogate PVS measurements. This is because PVS measures on T1W images are confounded e.g. by mineral deposition and vessel calcification, particularly in the BG, T1W signal is also affected by WMH, and is less sensitive to small PVS than T2W images. It is possible that a younger and healthier sample, where BG mineral and vessel calcification are less prevalent, might be less affected by this problem. On the other hand, a main interest in PVS is their role in ageing and neurodegeneration, meaning that accurate reliable PVS measurement in older people with brain pathology is important.

Caution is, therefore, recommended if PVS measurements from T1W and T2W are to be analysed together (e.g. in meta-analyses), because PVS computational measurements from these two imaging sequences do not necessarily reflect the same type of features. More research is needed to find ways to reduce the effect of potential confounds on PVS measurements where T1W is the only sequence available. Meantime, studies using T1W imaging to measure PVS should be aware of the limitations of sensitivity and the potential confounds when drawing conclusions on PVS associations with demographic, clinical or cognitive variables.

4.4. Strengths, limitations and future work

On a large and representative sample of individuals with small vessel disease and, therefore, potentially confounding pathological features, we have evaluated a state-of-the-art PVS segmentation method to inform recommendations on their implementation and usage, and document its

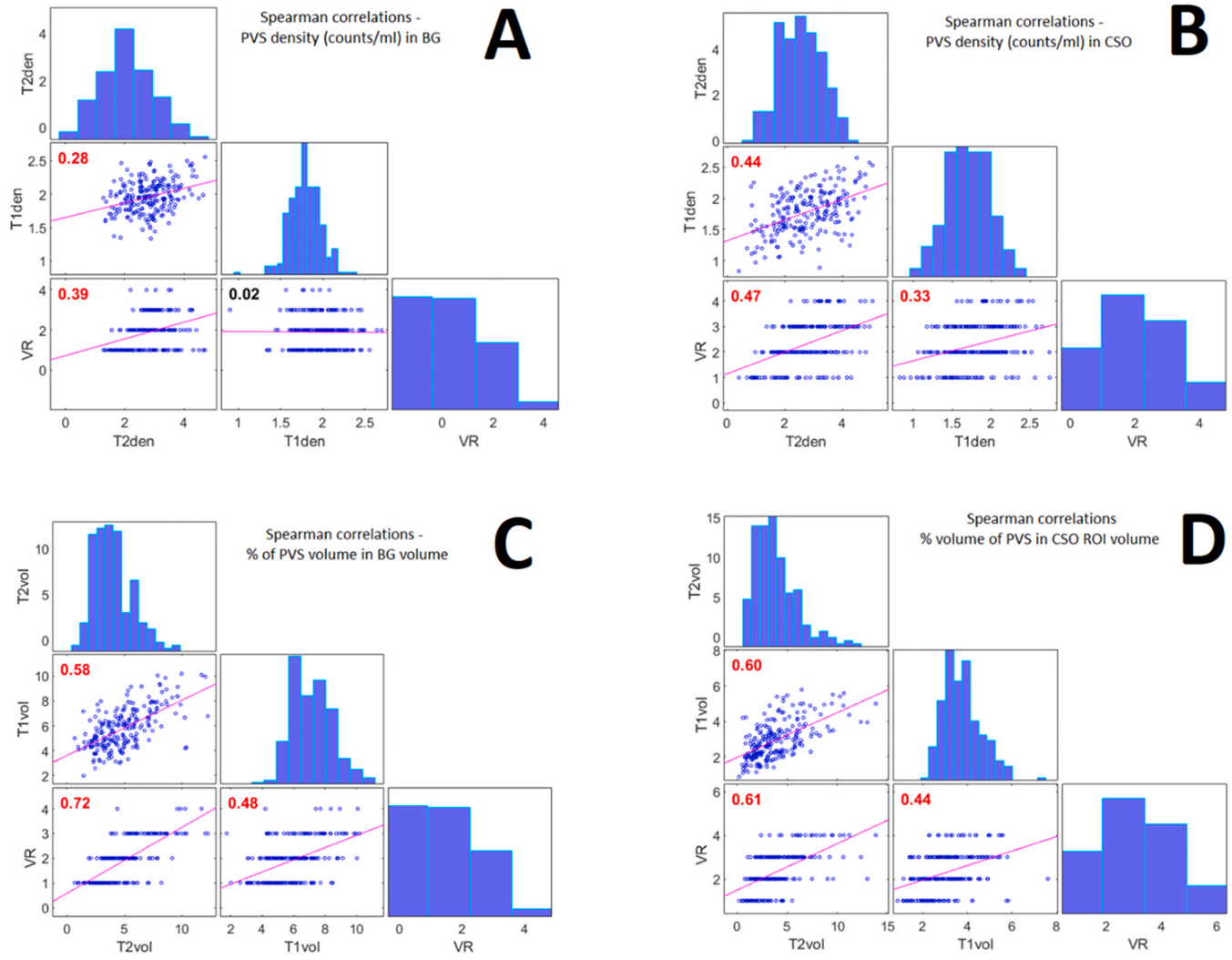

Fig. 8. Spearman rank cross-correlations between PVS visual scores (VR) and PVS counts/ml (i.e., T1den, T2den) in basal ganglia (A), centrum semiovale (B), PVS volume (i.e., T1vol, T2vol) as % in basal ganglia volume (C), and PVS volume (i.e., T1vol, T2vol) as % in centrum semiovale volume (D).

Table 5
Results from exploring known associations between PVS and age, PVS and hypertension, and PVS and WMH for measurements from T1W and T2W (adjusting also for sex, high cholesterol and smoking) (n = 217).

Parameter (outcome variable)	Age			Hypertension			WMH (total Fazekas)		
	B	SE	p- value	B	SE	p-value	B	SE	p-value
BG PVS vol (T1W)	-0.008	0.0097	0.42	**0.68**	**0.22**	**0.002**	**0.51**	**0.070**	**< 0.0001**
BG PVS vol (T2W)	**0.069**	**0.012**	**< 0.0001**	**1.08**	**0.26**	**< 0.0001**	**0.57**	**0.083**	**< 0.0001**
BG PVS dens (T1W)	0.0021	0.0017	0.22	**0.083**	**0.038**	**0.030**	-0.004	0.012	0.74
BG PVS dens (T2W)	**0.021**	**0.0042**	**< 0.0001**	**0.27**	**0.094**	**0.0042**	**0.11**	**0.030**	**0.0002**
CSO PVS vol (T1W)	0.0025	0.0065	0.70	0.20	0.14	0.17	**0.36**	**0.047**	**< 0.0001**
CSO PVS vol (T2W)	**0.077**	**0.015**	**< 0.0001**	0.33	0.33	0.32	**0.49**	**0.10**	**< 0.0001**
CSP PVS dens (T1W)	*0.0050*	*0.0025*	*0.045*	*0.11*	*0.055*	*0.049*	0.0019	0.018	0.91
CSO PVS dens (T2W)	**0.040**	**0.0058**	**< 0.0001**	**0.27**	**0.13**	**0.035**	**0.10**	**0.041**	**0.012**

performance on common situations: inter-observer differences, different image normalisation strategies, lack of the ideal sequence for identifying PVS, and variations in image quality. Table 6 summarises our main recommendations for best practices in the application of this method, and for achieving relatively robust and high-quality results in the STRIVE-2-recommended scenario (i.e., PVS identification in T2-weighted images).

Despite emerging deep learning schemes having shown encouraging results (i.e., critically reviewed in Pham et al., 2022), the widespread application of such advanced artificial intelligence (AI) methods is still hampered by well-known difficulties in which the international community of computer scientists is still working, namely a) underperformance in out-of-distribution samples, b) incorporation of a meaningful measure of uncertainty in the results, c) heterogeneity and inadequateness of the loss functions used, d) lack of an optimal quality measure for their evaluation, e) lack of interpretability of the wrong outputs, for just mentioning a few. This confers to the method evaluated, and, therefore, to our analyses, long-lasting validity in the clinical research if PVS are to be assessed. However, still exist both false positives and false negatives in PVS segmentations, meaning that

Table 6
Summary of main recommendations.

Topic	Recommendation
Image normalisation	Normalise the image intensities of the whole brain-extracted image prior to the application of the vesselness filter (i.e., excluding skull and extra-cranial tissues, but including cerebrospinal fluid-filled regions). Adding post-filtering normalisation confers robustness to threshold selection against inter-observer variations.
Threshold adjustment	Threshold the (vesselness) filter responses separately in each region of interest (ROI) (i.e., basal ganglia and centrum semiovale)
Base MRI sequence	T2W is the preferred sequence to segment PVS. Although this method (as described) is vulnerable to elongated focal T2W hyperintensities of other nature, PVS segmentations in T1W may be corrupted by additional confounding pathology (i.e., vessel calcifications) for which this method is not discriminatory.
Presence of noise	Identify noisy images prior to segmenting PVS, as differential thresholding per ROI depending on image quality is necessary (i.e., for example for T2W images: low quality – higher thresholds; high-quality – comparatively lower thresholds in general)
Parameters to identify noisy T1W and T2W images (from mriqc)	Entropy Focus Criterion, Mortamet's quality indexes, Signal to Noise Ratio (SNR) in tissue, Dietrich's SNR, and summary stats for background. For T2W images, additionally, white-matter to maximum intensity ratio, and Intensity Non-Uniformity (see considerations inSupplementary material)
Hessian-based vesselness filter	The Frangi filter is preferred over the Jerman filter. Although both filters lead to similar results, the Frangi filter has more degrees of freedom that one can leverage to be more or less strict on what could be a PVS morphologically-speaking and what is not.
Discrimination from lacunes	In addition to the optimisation of the vesselness filter parameters, apply k-means clustering to large elongated clusters to separate clustered PVS.

encouraging statistical results are not necessarily indicative of good segmentation, given that they can effectively cancel each other out in PVS counts. Ultimately, visual validations are likely to remain important, even on a subsample if datasets are large, to prevent any misleading statistical results. Important aspects are yet to be investigated thoroughly: equivalency between assessments that use images acquired at different magnetic field strengths (e.g., 1.5 T vs. 3 T and 7 T), accuracy in longitudinal measurements at individual and group levels, and correspondence between results from images acquired at different spatial resolutions (i.e., 3D vs. 2D).

Author contributions

MVH: Conceptualization, data curation, formal analysis, investigation, methodology, software, validation, visualization, writing - original draft, writing -review and editing, RDC: investigation, software, validation, writing - review and editing, LB: investigation, methodology, software, validation, writing - review and editing, data curation, JB: formal analysis, investigation, methodology, software, validation, visualization, writing - review and editing, WX: data curation, formal analysis, investigation, methodology, validation, visualization, writing -review and editing, YC, DJG, CAR, JFZ, XL, WH, SJW, UC, AJ, FD: data curation, formal analysis, investigation, validation, writing - review and editing, MS, MJT: conceptualization, data curation and collection, writing - review and editing, RB: Project administration, resources, writing - review and editing, JMW: Investigation, funding acquisition, methodology, supervision, resources, writing - review and editing.

CRediT authorship contribution statement

Jochems Angela: Writing – review & editing, Validation, Investigation, Formal analysis, Data curation. **Wiseman Stewart:** Writing – review & editing, Validation, Investigation, Formal analysis, Data curation. **Chappell Francesca:** Writing – review & editing, Supervision, Investigation, Data curation. **Doubal Fergus:** Writing – review & editing, Validation, Investigation, Formal analysis, Data curation. **Cheng Yajun:** Writing – review & editing, Validation, Investigation, Formal analysis, Data curation. **Thrippleton Michael:** Writing – review & editing, Validation, Methodology, Investigation, Formal analysis, Data curation. **Ballerini Lucia:** Writing – review & editing, Validation, Software, Methodology, Investigation, Data curation. **Jaime García Daniela:** Writing – review & editing, Validation, Investigation, Formal analysis, Data curation. **Arteaga Reyes Carmen:** Writing – review & editing, Validation, Investigation, Formal analysis, Data curation. **Brown Rosalind:** Writing – review & editing, Resources, Project administration. **Wardlaw Joanna:** Writing – review & editing, Validation, Supervision, Resources, Project administration, Methodology, Investigation, Funding acquisition. **Clancy Una:** Writing – review & editing, Validation, Methodology, Investigation, Formal analysis, Data curation. **Hewins Will:** Writing – review & editing, Validation, Investigation, Formal analysis, Data curation. **Xu William:** Writing – review & editing, Visualization, Validation, Methodology, Investigation, Formal analysis, Data curation. **Stringer Michael:** Writing – review & editing, Validation, Investigation, Formal analysis, Data curation. **Bernal José:** Writing – review & editing, Visualization, Validation, Software, Methodology, Investigation, Formal analysis. **Zhang Jun-Fang:** Writing – review & editing, Validation, Investigation, Formal analysis, Data curation. **Valdés Hernández Maria:** Writing – original draft, Visualization, Validation, Software, Methodology, Investigation, Formal analysis, Data curation, Conceptualization. **Liu Xiaodi:** Writing – review & editing, Validation, Investigation, Formal analysis, Data curation. **Duarte Coello Roberto:** Writing – review & editing, Validation, Software, Investigation.

Declaration of Competing Interest

The authors declare that they have no known competing financial interests or personal relationships that could have appeared to influence the work reported in this paper.

Data availability

Data will be made available on request.

Acknowledgements

We thank all those involved with the Mild Stroke Study 3, including the participants, their families, nurses, clinicians, researchers and support staff, without whom the data utilised in this project would not have been available.

This study is partially funded by the Hilary and Galen Weston Foundation under the Novel Biomarkers 2019 scheme (ref UB190097) administered by the Weston Brain Institute. The Mild Stroke Study 3 is partially supported by the UK Dementia Research Institute which receives its funding from DRI Ltd, funded by the UK MRC, Alzheimer's Society and Alzheimer's Research UK. This study received also funds from the Fondation Leducq Network for the Study of Perivascular Spaces in Small Vessel Disease (16 CVD 05); Stroke Association 'Small Vessel Disease-Spotlight on Symptoms (SVD-SOS)'(SAPG 19\100068; the MRC Doctoral Training Programme in Precision Medicine (JB);The Row Fogo Charitable Trust (MCVH, FMC) (BRO-D.FID3668413); Stroke

Association Garfield Weston Foundation Senior Clinical Lectureship (FND) (TSALECT 2015/04); NHS Research Scotland (FND); Stroke Association Post-Doctoral Fellowship (SW) (SAPDF 18/100026); British Heart Foundation Edinburgh Centre for Research Excellence (RE/18/5/34216); NHS Lothian Research and Development Office (MJT); Alzheimer's Netherlands (ACCJ); Chief Scientist Office of Scotland Clinical Academic Fellowship (UC) (CAF/18/08); Stroke Association Princess Margaret Research Development Fellowship (UC) (2018). The 3 T MR scanner is funded by the Wellcome Trust (104916/Z/14/Z), Dunhill Trust (R380R/1114), Edinburgh and Lothians Health Foundation (2012/17), Muir Maxwell Research Fund and the University of Edinburgh.

Appendix A. Supporting information

Supplementary data associated with this article can be found in the online version at doi:10.1016/j.jneumeth.2023.110037.

References

Aribisala, B.S., Riha, R.L., Valdes Hernandez, M., Muñoz Maniega, S., Cox, S., Radakovic, R., Taylor, A., Pattie, A., Corley, J., Redmond, P., Bastin, M.E., Starr, J., Deary, I., Wardlaw, J.M., 2020. Sleep and brain morphological changes in the eighth decade of life (Jan). Sleep. Med 65, 152–158. https://doi.org/10.1016/j.sleep.2019.07.015. Epub 2019 Jul 24.

Aribisala, B.S., Valdés Hernández, M.D.C., Okely, J.A., Cox, S.R., Ballerini, L., Dickie, D. A., Wiseman, S.J., Riha, R.L., Muñoz Maniega, S., Radakovic, R., Taylor, A., Pattie, A., Corley, J., Redmond, P., Bastin, M.E., Deary, I., Wardlaw, J.M., 2023. Sleep quality, perivascular spaces and brain health markers in ageing - A longitudinal study in the Lothian Birth Cohort 1936 (Jun). Sleep. Med 106, 123–131. https://doi.org/10.1016/j.sleep.2023.03.016. Epub 2023 Mar 16.

Ballerini, L., Lovreglio, R., Hernández, M.D.C.V., Gonzalez-Castro, V., Maniega, S.M., Pellegrini, E., Bastin, M.E., Deary, I.J., Wardlaw, J.M., 2016. Application of the ordered logit model to optimising frangi filter parameters for segmentation of perivascular spaces. Procedia Comput. Sci. 90, 61–67. https://doi.org/10.1016/J.PROCS.2016.07.011.

Ballerini, L., Lovreglio, R., Valdés Hernández, M.D.C., Ramirez, J., Macintosh, B.J., Black, S.E., Wardlaw, J.M., 2018. Perivascular spaces segmentation in brain MRI using optimal 3D filtering. Sci. Rep. 8 https://doi.org/10.1038/s41598-018-19781-5.

Ballerini, L., Booth, T., Valdes Hernandez, M.D.C., Wiseman, S., Lovreglio, R., Munoz Maniega, S., Morrist, Z., Pattie, A., Corley, J., Gow, A., et al., 2020. Computational quantification of brain perivascular space morphologies: associations with vascular risk factors and white matter hyperintensities. A study in the Lothian Birth Cohort 1936. Neuroimage Clin. 25 https://doi.org/10.1016/j.nicl.2019.102120.

Barisano, G., Sheikh-Bahaei, N., Law, M., Toga, A.W., Sepehrband, F., 2021. Body mass index, time of day and genetics affect perivascular spaces in the white matter. J. Cereb. Blood Flow. Metab. 41 (7), 1563–1578.

Barnes, A., Ballerini, L., Valdés Hernández, M.D.C., Chappell, F.M., Muñoz Maniega, S., Meijboom, R., Backhouse, E.V., Stringer, M.S., Duarte Coello, R., Brown, R., Bastin, M.E., Cox, S.R., Deary, I.J., Wardlaw, J.M., 2022. Topological relationships between perivascular spaces and progression of white matter hyperintensities: a pilot study in a sample of the Lothian Birth Cohort 1936. Front. Neurol. 13, 889884 https://doi.org/10.3389/fneur.2022.889884.

Bernal, J., Valdés-Hernández, M.D.C., Escudero, J., Duarte, R., Ballerini, L., Bastin, M.E., Deary, I.J., Thrippleton, M.J., Touyz, R.M., Wardlaw, J.M., 2022. Assessment of perivascular space filtering methods using a three-dimensional computational model (Nov). Magn. Reson Imaging 93, 33–51. https://doi.org/10.1016/j.mri.2022.07.016. Epub 2022 Aug 4.

Bernal, J., Valdés Hernández, M., Ballerini, L., Escudero, J., Jochems, A.C.C., Clancy, U., Doubal, F.N., Stringer, M.S., Thrippleton, M.J., Touyz, R.M., Wardlaw, J.M. (2020). A Framework for Jointly Assessing and Reducing Imaging Artefacts Automatically Using Texture Analysis and Total Variation Optimisation for Improving Perivascular Spaces Quantification in Brain Magnetic Resonance Imaging. In: Medical Image Understanding and Analysis, pp. 171–183, edited by Papież, B.W., Namburete, A.I. L., Yaqub, M., Noble, J.A. (2020). Cham: Springer International Publishing.

Bernal, J., Xu, W., Valdés Hernández, M., Escudero, J., Jochems, A.C.C., Clancy, U., Doubal, F.N., Stringer, M.S., Thrippleton, M.J., Touyz, R.M., Wardlaw, J.M. 2021 Selective motion artefact reduction via radiomics and k-space reconstruction for improving perivascular space quantification in brain magnetic resonance imaging. in preparation in: Medical Image Understanding and Analysis. (2021). Springer International Publishing.

Boespflug, E.L., Schwartz, D.L., Lahna, D., Pollock, J., Iliff, J.J., Kaye, J.A., Rooney, W., Silbert, L.C., 2018. MR Imaging–based multimodal autoidentification of perivascular spaces (mMAPS): automated morphologic segmentation of enlarged perivascular spaces at clinical field strength. Radiology 286, 632–642.

Boutinaud, P., Tsuchida, A., Laurent, A., Adonias, F., Hanifehlou, Z., Nozais, V., Verrecchia, V., Lampe, L., Zhang, J., Zhu, Y.C., Tzourio, C., Mazoyer, B., Joliot, M., 2021. 3D Segmentation of perivascular spaces on T1-Weighted 3 Tesla MR images with a convolutional autoencoder and a U-shaped neural network. Front. Neuroinformatics 15, 29. https://doi.org/10.3389/FNINF.2021.641600/BIBTEX.

Brown, R., Benveniste, H., Black, S.E., Charpak, S., Dichgans, M., Joutel, A., Nedergaard, M., Smith, K.J., Zlokovic, B.V., Wardlaw, J.M., 2018. Understanding the role of the perivascular space in cerebral small vessel disease. Cardiovasc. Res. 114, 1462–1473.

C.H. Sudre K. Van Wijnen F. Dubost H. Adams D. Atkinson F. Barkhof M.A. Birhanu E.E. Bron R. Camarasa N. Chaturvedi Y. Chen Z. Chen S. Chen Q. Dou T. Evans I. Ezhov H. Gao M. Girones Sanguesa J. Domingo Gispert the ALFA study, for 2021Where Is. VALDO? Vasc. Lesions Detect. Segm. Chall. MICCAI 2022 doi: 10.48550/arxiv.2208.07167.

Choi, Y., Nam, Y., Choi, Y., Kim, J., Jang, J., Ahn, K.J., Kim, B. soo, Shin, N.Y., 2020. MRI-visible dilated perivascular spaces in healthy young adults: a twin heritability study. Hum. Brain Mapp. 41 (18), 5313–5324. https://doi.org/10.1002/HBM.25194.

Clancy, U., Garcia, D.J., Stringer, M.S., Thrippleton, M.J., Valdés-Hernández, M.C., Wiseman, S., Hamilton, O.K., Chappell, F.M., Brown, R., Blair, G.W., Hewins, W., Sleight, E., Ballerini, L., Bastin, M.E., Maniega, S.M., MacGillivray, T., Hetherington, K., Hamid, C., Arteaga, C., Morgan, A.G., Manning, C., Backhouse, E., Hamilton, I., Job, D., Marshall, I., Doubal, F.N., Wardlaw, J.M., 2021. Rationale and design of a longitudinal study of cerebral small vessel diseases, clinical and imaging outcomes in patients presenting with mild ischaemic stroke: Mild Stroke Study 3. Eur. Stroke J. 6 (1), 81–88.

Descombes, X., Kruggel, F., Wollny, G., Gertz, H.J., 2004. An object-based approach for detecting small brain lesions: application to virchow-robin spaces. IEEE Trans. Med. Imaging 23 (2), 246–255. https://doi.org/10.1109/TMI.2003.823061.

Doubal, F.N., MacLullich, A.M.J., Ferguson, K.J., Dennis, M.S., Wardlaw, J.M., 2010. Enlarged perivascular spaces on MRI are a feature of cerebral small vessel disease. Stroke 41, 450–454.

Duering, M., Biessels, G.J., Brodtmann, A., Chen, C., Cordonnier, C., de Leeuw, F.E., Debette, S., Frayne, R., Jouvent, E., Rost, N.S., Ter Telgte, A., Al-Shahi Salman, R., Backes, W.H., Bae, H.J., Brown, R., Chabriat, H., De Luca, A., deCarli, C., Dewenter, A., Doubal, F.N., Ewers, M., Field, T.S., Ganesh, A., Greenberg, S., Helmer, K.G., Hilal, S., Jochems, A.C.C., Jokinen, H., Kuijf, H., Lam, B.Y.K., Lebenberg, J., MacIntosh, B.J., Maillard, P., Mok, V.C.T., Pantoni, L., Rudilosso, S., Satizabal, C.L., Schirmer, M.D., Schmidt, R., Smith, C., Staals, J., Thrippleton, M.J., van Veluw, S.J., Vemuri, P., Wang, Y., Werring, D., Zedde, M., Akinyemi, R.O., Del Brutto, O.H., Markus, H.S., Zhu, Y.C., Smith, E.E., Dichgans, M., Wardlaw, J.M., 2023. Neuroimaging standards for research into small vessel disease-advances since 2013 (Jul). Lancet Neurol. 22 (7), 602–618. https://doi.org/10.1016/S1474-4422(23)00131-X. Epub 2023 May 23.

Duperron, M.G., Knol, M.J., Le Grand, Q., et al., 2023. Genomics of perivascular space burden unravels early mechanisms of cerebral small vessel disease. Nat. Med. 29, 950–962. https://doi.org/10.1038/s41591-023-02268-w.

Fazekas, F., Chawluk, J.B., Alavi, A., Hurtig, H.I., Zimmerman, R.A., 1987. MR signal abnormalities at 1.5 T in Alzheimer's dementia and normal aging, 351-6 AJR Am. J. Roentgenol. 149 (2). https://doi.org/10.2214/ajr.149.2.351.

Francis, F., Ballerini, L., Wardlaw, J.M., 2019. Perivascular spaces and their associations with risk factors, clinical disorders and neuroimaging features: a systematic review and meta-analysis. Int. J. Stroke 14, 359–371.

Frangi, A.F., Niessen, W.J., Vincken, K.L., Viergever, M.A., 1998. Multiscale vessel enhancement filtering. In: Wells, W.M., Colchester, A., Delp, S. (Eds.), edited by, Medical Image Computing and Computer-Assisted Intervention — MICCAI'98. Springer Berlin Heidelberg, Berlin, Heidelberg, pp. 130–137.

Godenschweger, F., Kägebein, U., Stucht, D., Yarach, U., Sciarra, A., Yakupov, R., Lüsebrink, F., Schulze, P., Speck, O., 2016. Motion correction in MRI of the brain. Phys. Med Biol. 61 (5), R32–56. https://doi.org/10.1088/0031-9155/61/5/R32. Epub 2016 Feb 11.

Hamilton, O.K.L., Cox, S.R., Okely, J.A., Conte, F., Ballerini, L., Bastin, M.E., Corley, J., Taylor, A.M., Page, D., Gow, A.J., Muñoz Maniega, S., Redmond, P., Valdés-Hernández, M., del, C., Wardlaw, J.M., Deary, I.J., 2021. Cerebral small vessel disease burden and longitudinal cognitive decline from age 73 to 82: the Lothian Birth Cohort 1936, 2021 11:1 Transl. Psychiatry 11 (1), 1–12. https://doi.org/10.1038/s41398-021-01495-4.

Huang, P., Zhu, Z., Zhang, R., Wu, X., Jiaerken, Y., Wang, S., Yu, W., Hong, H., Lian, C., Li, K., Zeng, Q., Luo, X., Xu, X., Yu, X., Yang, Y., Zhang, M., 2021b. Factors associated with the dilation of perivascular space in healthy elderly subjects. Frontiers in Aging Neuroscience 13, 125. https://doi.org/10.3389/FNAGI.2021.624732.

Jerman, T., Pernus, F., Likar, B., Spiclin, Z., 2016. Enhancement of vascular structures in 3D and 2D angiographic images. IEEE Trans. Med. Imaging 35, 2107–2118.

Jessen, N.A., Munk, A.S.F., Lundgaard, I., Nedergaard, M., 2015. The glymphatic system: a beginner's guide. Neurochem. Res. 40, 2583–2599.

Kruggel, F., Chalopin, C., Descombes, X., Kovalev, V., Rajapakse, J.C. 2002. Segmentation of pathological features in MRI brain datasets. ICONIP 2002 - Proceedings of the 9th International Conference on Neural Information Processing: Computational Intelligence for the E-Age, 5, 2673–2677. https://doi.org/10.1109/ICONIP.2002.1201981.

Lamy, J., Merveille, O., Kerautret, B., Passat, N., Vacavant, A. 2021. Vesselness filters: A survey with benchmarks applied to liver imaging. In: International Conference on Pattern Recognition (ICPR).

Lian, C., Zhang, J., Liu, M., Zong, X., Hung, S.C., Lin, W., Shen, D., 2018. Multi-channel multi-scale fully convolutional network for 3D perivascular spaces segmentation in 7T MR images. Med. Image Anal. 46, 106–117. https://doi.org/10.1016/J.MEDIA.2018.02.009.

Liu, C., Habib, T., Salimeen, M., Pradhan, A., Singh, M., Wang, M., Wu, F., Zhang, Y., Gao, L., Yang, G., Li, X., Yang, J., 2020. Quantification of visible Virchow–Robin spaces for detecting the functional status of the glymphatic system in children with newly diagnosed idiopathic generalized epilepsy. Seizure 78, 12–17. https://doi.org/10.1016/j.seizure.2020.02.015.

Liu, S., Hou, B., You, H., Zhang, Y., Zhu, Y., Ma, C., Zuo, Z., Feng, F., 2021. The association between perivascular spaces and cerebral blood flow, brain volume, and cardiovascular risk. Front Aging Neurosci. 13, 599724 https://doi.org/10.3389/fnagi.2021.599724.

McRobbie, D.W., Moore, E.A., Graves, M.J., Prince, M.R. (2006). MRI From Picture to Proton, 2nd Ed, Cambridge: Cambridge University Press.

Mestre, H., Kostrikov, S., Mehta, R.I., Nedergaard, M., 2017. Perivascular spaces, glymphatic dysfunction, and small vessel disease. Clin. Sci. 131, 2257–2274.

Moses, J., Sinclair, B., Schwartz, D.L., Silbert, L.C., O'Brien, T.J., Law, M., Vivash, L., 2022. Perivascular spaces as a marker of disease severity and neurodegeneration in patients with behavioral variant frontotemporal dementia. Front. Neurosci. 16 https://doi.org/10.3389/FNINS.2022.1003522.

Moses, J., Sinclair, B., Law, M., O'Brien, T.J., Vivash, L., 2023. Automated methods for detecting and quantitation of enlarged perivascular spaces on MRI. J. Magn. Reson. Imaging 57 (1), 11–24. https://doi.org/10.1002/JMRI.28369.

Niazi, M., Karaman, M., Das, S., Zhou, X.J., Yushkevich, P., Cai, K., 2018. Quantitative MRI of perivascular spaces at 3T for early diagnosis of mild cognitive impairment. Am. J. Neuroradiol. 39 (9), 1622–1628. https://doi.org/10.3174/AJNR.A5734.

Park, S.H., Zong, X., Gao, Y., Lin, W., Shen, D., 2016. Segmentation of perivascular spaces in 7 T MR image using auto-context model with orientation-normalized features. NeuroImage 134, 223–235. https://doi.org/10.1016/J.NEUROIMAGE.2016.03.076.

Pham, W., Lynch, M., Spitz, G., O'Brien, T., Vivash, L., Sinclair, B., Law, M., 2022. A critical guide to the automated quantification of perivascular spaces in magnetic resonance imaging. Dec 14 Front. Neurosci. 16, 1021311. https://doi.org/10.3389/fnins.2022.1021311.

Piantino, J., Schwartz, D.L., Luther, M., Newgard, C., Silbert, L., Raskind, M., Pagulayan, K., Kleinhans, N., Iliff, J., Peskind, E., 2021. Link between Mild traumatic brain injury, poor sleep, and magnetic resonance imaging: visible perivascular spaces in veterans. J. Neurotrauma 38 (17), 2391–2399.

Potter, G.M., Chappell, F.M., Morris, Z., Wardlaw, J.M., 2015a. Cerebral perivascular spaces visible on magnetic resonance imaging: development of a qualitative rating scale and its observer reliability. Cerebrovasc. Dis. 39, 224–231.

Potter, G.M., Doubal, F.N., Jackson, C.A., Chappell, F.M., Sudlow, C.L., Dennis, M.S., Wardlaw, J.M., 2015b. Enlarged perivascular spaces and cerebral small vessel disease. Int. J. Stroke 10, 376–381.

Schwartz, D.L., Boespflug, E.L., Lahna, D.L., Pollock, J., Roese, N.E., Silbert, L.C., 2019. Autoidentification of perivascular spaces in white matter using clinical field strength T1 and FLAIR MR imaging. NeuroImage 202, 116126. https://doi.org/10.1016/J.NEUROIMAGE.2019.116126.

Sepehrband, F., Barisano, G., Sheikh-Bahaei, N., et al., 2019. Image processing approaches to enhance perivascular space visibility and quantification using MRI. Sci. Rep. 9, 12351 https://doi.org/10.1038/s41598-019-48910-x.

Sepehrband, F., Barisano, G., Sheikh-Bahaei, N., Choupan, J., Cabeen, R.P., Lynch, K.M., Crawford, M.S., Lan, H., Mack, W.J., Chui, H.C., Ringman, J.M., Toga, A.W., 2021. Volumetric distribution of perivascular space in relation to mild cognitive impairment. Neurobiol. Aging 99, 28–43. https://doi.org/10.1016/J.NEUROBIOLAGING.2020.12.010.

Shaw, R., Sudre, C.H., Varsavsky, T., Ourselin, S., Cardoso, M.J., 2020. A k-Space model of movement artefacts: application to segmentation augmentation and artefact removal. IEEE Trans. Med. Imaging 39, 2881–2892.

Spijkerman, J.M., Zwanenburg, J.J.M., Bouvy, W.H., Geerlings, M.I., Biessels, G.J., Hendrikse, J., Luijten, P.R., Kuijf, H.J., 2022. Automatic quantification of perivascular spaces in T2-weighted images at 7 T MRI. Cereb. Circ. Cogn. Behav. 3, 100142 https://doi.org/10.1016/J.CCCB.2022.100142.

Uchiyama, Y., Kunieda, T., Asano, T., Kato, H., Hara, T., Kanematsu, M., Iwama, T., Hoshi, H., Kinosada, Y., Fujita, H. 2008. Computer-aided diagnosis scheme for classification of lacunar infarcts and enlarged Virchow-Robin spaces in brain MR images. Proceedings of the 30th Annual International Conference of the IEEE Engineering in Medicine and Biology Society, EMBS'08 - "Personalized Healthcare through Technology," 3908–3911. https://doi.org/10.1109/IEMBS.2008.4650064.

Valdés Hernández, M., Ballerini, L., Glatz, A., Muñoz Maniega, S., Gow, A.J., Bastin, M. E., Starr, J.M., Deary, I.J., Wardlaw, J.M., 2020. Perivascular spaces in the centrum semiovale at the beginning of the 8th decade of life: effect on cognition and associations with mineral deposition. Brain Imaging Behav. 14, 1865–1875.

Valdés Hernández, M.D.C., Piper, R.J., Wang, X., Deary, I.J., Wardlaw, J.M., 2013. Towards the automatic computational assessment of enlarged perivascular spaces on brain magnetic resonance images: a systematic review. J. Magn. Reson. Imaging 38, 774–785. https://doi.org/10.1002/jmri.24047.

Valdés Hernández C. Maria del Ballerini Lucia Glatz Andreas S. Aribisala, Benjamin Bastin Mark E. Dickie David Alexander Duarte Coello Roberto Munoz Maniega Susana Wardlaw M. Joanna Step-by-step pipeline for segmenting enlarged perivascular spaces from 3D T2-weighted MRI, 2018–2023 [software]. University of Edinburgh. College of Medicine and Veterinary Medicine. Centre for Clinical Brain Sciences 2023 doi: 10.7488/ds/7486.

van Wijnen, K.M.H., Dubost, F., Yilmaz, P., Ikram, M.A., Niessen, W.J., Adams, H., Vernooij, M.W., de Bruijne, M., 2019. Automated lesion detection by regressing intensity-based distance with a neural network. Lecture Notes in Computer Science (Including Subseries Lecture Notes in Artificial Intelligence and Lecture Notes in Bioinformatics), 11767. LNCS 234–242. https://doi.org/10.1007/978-3-030-32251-9_26/TABLES/1.

Vikner, T., Karalija, N., Eklund, A., Malm, J., Lundquist, A., Gallewicz, N., Dahlin, M., Lindenberger, U., Riklund, K., Bäckman, L., Nyberg, L., Wåhlin, A., 2022. 5-Year Associations among cerebral arterial pulsatility, perivascular space dilation, and white matter lesions. Ann. Neurol. https://doi.org/10.1002/ANA.26475.

Wang, S., Huang, P., Zhang, R., Hong, H., Jiaerken, Y., Lian, C., Yu, X., Luo, X., Li, K., Zeng, Q., Xu, X., Yu, W., Wu, X., Zhang, M., 2021. Quantity and morphology of perivascular spaces: associations with vascular risk factors and cerebral small vessel disease. J. Magn. Reson. Imaging 54 (4), 1326–1336. https://doi.org/10.1002/JMRI.27702.

Wardlaw, J.M., Smith, E.E., Biessels, G.J., Cordonnier, C., Fazekas, F., Frayne, R., Lindley, R.I., O'Brien, J.T., Barkhof, F., Benavente, O.R., et al., 2013. Neuroimaging standards for research into small vessel disease and its contribution to ageing and neurodegeneration. Lancet Neurol. 12, 822–838.

Wardlaw, J.M., Benveniste, H., Nedergaard, M., Zlokovic, B.V., Mestre, H., Lee, H., Douba, l F.N., Brown, R., Ramirez, J., Macintosh, B.J., et al., 2020. Perivascular spaces in the brain: anatomy, physiology and pathology. Nat. Rev. Neurol. 16, 137–153.

Wood, M.L., Henkelman, R.M., 1985. MR image artifacts from periodic motion: MR image artifacts from motion. Med. Phys. 12, 143–151.

Zaitsev, M., Maclaren, J., Herbst, M., 2015. Motion artifacts in MRI: a complex problem with many partial solutions: motion artifacts and correction. J. Magn. Reson. Imaging 42, 887–901.

Zhang, Y., Brady, M., Smith, S., 2001. Segmentation of brain MR images through a hidden Markov random field model and the expectation-maximization algorithm. IEEE Trans Med Imag 20 (1), 45–57.

Zhang, J., Gao, Y., Park, S.H., Zong, X., Lin, W., Shen, D., 2017. Structured learning for 3-D perivascular space segmentation using vascular features. IEEE Trans. Biomed. Eng. 64 (12), 2803–2812. https://doi.org/10.1109/TBME.2016.2638918.